Profile Analysis of Regularly Microstructured Surfaces

H. Payer[1], T. Haschke[1], R. Reichardt[1], G. Li[2], K. Graf[2,3] and W. Wiechert[1,3]

Abstract: Microstructured surfaces are of steadily increasing importance in a large variety of technological applications. For the purpose of quality assurance, e.g. during variation studies of experimental parameters or for comparison with results from simulations, the surface geometry must be precisely measured and described in terms of geometric parameters. An analysis tool for regularly structured surfaces is presented that performs a highly automated evaluation of surface scanning data and derives geometric quality control parameters. To demonstrate the power of the analysis tool it is exemplarily applied for the investigation of microcraters emerging after the evaporation of micrometer-sized toluene droplets on a polystyrene substrate. The shape of the craters is described by a mathematical model under the assumption of rotational or elliptic symmetry. The ideal geometry generated from this model is called a synthetic surface. Mismatch between the synthetic and the experimentally determined surface morphology is then minimized by means of a full least squares fitting. In order to characterize the crater profile global geometrical parameters are derived and used for an automated statistical analysis subsequent to the fitting procedure. An evaluation example is presented for two sets of 20 microcraters each and the reproducibility of the shapes of the craters is discussed.

Keyword: profile analysis, microstructured polymer surfaces, drop evaporation, optical profilometry, high throughput screening.

[1] University of Siegen, Department of Simulation, Siegen, Germany
[2] Max Planck Institute for Polymer Research, Polymer Physics Group, Mainz, Germany
[3] Corresponding authors: wolfgang.wiechert@uni-siegen.de (simulations); grafk@mpip-mainz.mpg.de (experiments)

1 Introduction

Microstructured surfaces gain importance in a large variety of applications. Examples occur in architectural glazings [Hoßfeld; Wittwer; Nitz; Gombert; Bläsi; Bühler; Walze and Georg (2003)], in tribological modifications of materials [Alberdi; Merino; Barragia and Aranzabe (2004)] or in general for Lab-on-Chip applications. Here, they can be used as microvessels [Bonaccurso; Butt and Graf (2004)], as components for micro-flow devices [Shastry; Case and Böhringer (2006)], for chemical analysis, e.g. of DNA [Osfouri; Stano and Luisi (2005)], for platforms of cell-based biosensors [Krol; Nolte; Diaspro; Mazza; Magrassi; Gliozzi and Fery (2005)] or for studying physico-chemical effects at the micro- and nanoscale [Bonaccurso; Butt and Graf (2004); Bonaccurso and Graf (2004); Li; Butt and Graf (2006); Li; Höhn and Graf (2006); Lipowsky (2004); Stupperich-Sequeira; Graf and Wiechert (2006)]. To gain control over the fabrication and modification of microstructured surfaces it is necessary to analyse and characterize the surface morphology [Benitez; Minano and Hernandez (2004); Benitez; Minano and Santamaria (2006); Ichikawa and Toriwaki (1996); Kagerer; Brodmann; Valentin; Filzek and Popp (2002)].

Commonly, microstructured surfaces at the micro- and nanoscale are analyzed with atomic force microscopy (AFM) [Bonaccurso; Butt; Hankeln; Niesenhaus and Graf (2005); Magnani; Priamo; Pasqui and Barbucci (2003); Seemann; Brinkmann; Kramer; Lange and Lipowsky (2004)] or optical profilometry [Kagerer; Brodmann; Valentin; Filzek and Popp (2002); Valentin (2006)]. These techniques allow a detailed measurement of the surface morphology with sub-micrometer resolution. Usually, these methods

provide a large amount of data that is necessary to describe all details of the surface morphology. For example, an optical scan of a surface of 500 μm $\times$ 500 μm typically produces a 16 MB text file containing the *x*- and *y*-coordinates and the height information (*z*-coordinate) for each data point. With regard to further data processing, e.g. for a comparison with simulated data [Haschke; Wiechert; Graf; Bonaccurso; Li and Suttmeier (2007); Stupperich-Sequeira; Graf and Wiechert (2006)] this amount of data is rather difficult to handle. Thus, a necessary prerequisite for a fast and efficient data processing is a strong data reduction - with a simultaneous conservation of the most important surface features. Moreover, the reduced data set must be suited to reconstruct the substrates' surface in a fast and sufficient way.

Beside the data compression an analysis tool for microstructured surfaces should provide a subsequent statistical evaluation of the processed data. With the help of this statistics it is possible to

- prove the quality of the surface structures (quality assurance),

- estimate the reproducibility of the produced volumes (process accuracy),

- analyse empirically the influence of experimental parameters on the microstructure geometry (process control),

- study stochastic influences of process parameters on experiments on the microscale (reproducibility), and

- prepare experimental data for the comparison with simulations (computational engineering, cf. Figure 3 and Table 1).

Clearly, the problem of surface analysis also occurs for macroscopic structures. For this reason, the methods developed in the following can in principle be also applied in this case. However, there are some fundamental differences between the macroscopic and microscopic application: Macroscopic structures are usually created by mechanical tools (like e.g. embossing) that allow for a rather direct control of their geometry.

Usually, a blueprint of the structures is available which can be directly compared with its realization.
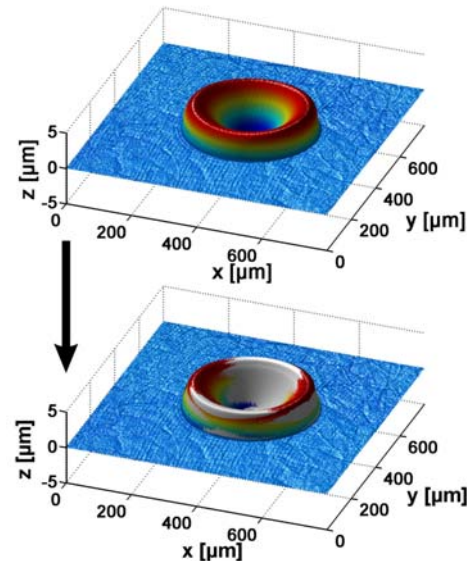

Figure 1: microcrater on a polystyrene substrate left after the evaporation of a sessile drop of toluene measured with 3D confocal white-light microscopy (μSurf®, Nanofocus AG, Oberhausen, Germany). Note the different scales on the axes. Bottom: comparison of the original (colored) and the synthetic crater (gray) for an exemplary data set. Colored and gray image are superposed and color appears where the original crater is overhanging the synthetic crater.

In contrast, the microstructures addressed in this work indirectly emerge from a complex interplay of different physico-chemical phenomena. Their geometry can only be influenced quite indirectly by general process parameters (see below for an example). Particularly, these microstructures have some kind of symmetry that is not necessarily present in the macroscopic case. Consequently, the tasks given in the above list and the geometric profile description developed in the following are rather typical for the microscopic case. For this reason the following parts focus on microstructures.

Additionally, this paper intends to provide a standard procedure for the analysis of microstructures to better understand the physics behind their for-

mation (in upcoming papers). This way, the presented tool does not only allow the characterization of surface structures but also provide a method to judge on the significance of different physico-chemical phenomena, which could be responsible for the structure formation.

We present a general approach for a computer-aided profile analysis of regularly shaped structures under the assumption of rotational or elliptic symmetry of each structured component. This is demonstrated exemplarily for polymer substrates made of polystyrene, which are regularly surface-structured by the deposition and evaporation of micrometer-sized toluene drops [Bonaccurso; Butt; Hankeln; Niesenhaus and Graf (2005); Li; Butt and Graf (2006)]. This way, flat concave structures (microcraters) are formed, which usually have a diameter of some ten to some hundred microns and an overall depth of some microns (cf. Fig.1, top, and [Bonaccurso; Butt; Hankeln; Niesenhaus and Graf (2005)]).

The process of microcrater formation can be described by the synergy of several physico-chemical processes. Basically, the effect resembles the formation of coffee-stains on a table: if a drop is evaporating on a surface there is a drag of the liquid and the solute to the outer rim if the drop stays pinned [Deegan; Bakajin; Dupont; Huber; Nagel and Witten (1997)]. Thus, material is accumulated at the rim of the droplet and, for a sessile drop of a solvent on a polymer, finally leads to a concave structure [Bonaccurso; Butt; Hankeln; Niesenhaus and Graf (2005); Sirringhaus; Kawase; Friend; Shimoda; Inbasekaran; Wu and Woo (2000)]. A simulation tool that accounts for these processes was developed by [Haschke; Wiechert; Graf; Bonaccurso; Li and Suttmeier (2007); Stupperich-Sequeira; Graf and Wiechert (2003); Stupperich-Sequeira; Graf and Wiechert (2006)]. Under the assumption of rotational symmetry, it is possible to simulate the evaporation process and the emergence of the microcraters.

For a comparison of simulated and experimental data it is essential to extract an average profile of the craters. Here we present a profile analysis procedure, which converts the experimen-

tal 3D profile into a small set of parameters describing the shape by a mathematical model (see chapter 3, *geometric model*). The crater reconstructed from the mathematical model is called "synthetic crater" (Fig.1, bottom). From these synthetic craters global geometric parameters are derived (cf. Fig.3, Tab.1), which facilitate the statistical analysis of the surface structures and enables the understanding of their formation.

In detail, the profile analysis procedure consists of the following steps, which are described in the different chapters below as indicated.

Part I: Pre-processing and determination of starting values for the consecutive optimization:	
1.	Identifying the craters within the matrix of raw data (appendix, step 1)
2.	Smoothing of experimental noise (appendix, step 2)
3.	Identifying the crater's centroid (appendix, step 3)
4.	Cutting of defined profiles (appendix, step 4)
5.	Pre-fitting of the raw data with a B-spline (appendix, step 5)
Part II: Parameter fitting procedure (optimization):	
6.	Comparison of raw data (*RD*) and the synthetic crater (*SC*) (full least squares fitting according to Eq.(6)) (chapter 3.4; appendix, step 6)
7.	Iteration step by re-adaptation of the B-spline parameters (genetic algorithm). Continue with step 6. (chapter 3.4; appendix, step 7)
Part III: Statistical Evaluation:	
8.	Determination of global geometric parameters (chapter 3.5; appendix, step 8)
9.	Statistical analysis of synthetic craters and subsequent serial analysis (chapter 4; appendix, step 9)

This profile analysis tool is implemented in Matlab [The Mathworks Inc. (2007)] and provides the results of the statistical evaluation (step 8) in text

files and Excel sheets, respectively.

The developed software tool allows the computation of the model parameters and the synthetic craters, especially with respect to a serial analysis of several experimental datasets, the reproduction of the original data and the reduction of the huge amount of experimental data. It will be shown that a data compression rate of approximately 67,000: 1 (16,080,000 Bytes : 240 Bytes) is realized. As an example, the results of the statistical analysis of two experiments with 20 craters each are shown in Table 2 and are discussed later on. Between the two experiments a new substrate was taken and the droplet dispenser was rearranged. This way, different sources of experimental errors can be identified.

2   Experimental Setup and Data Evaluation

The generation of the microcraters was performed with an experimental setup described in [Li; Höhn and Graf (2006)]. A droplet of a solvent is formed at the outlet of a vertically oriented syringe. After that the pendant droplet is deposited on a polymer surface by moving the polymer substrate into contact by an actuator until a liquid bridge is formed. Afterwards, the substrate is immediately retracted until rupture of the liquid bridge and the deposited drop evaporates in still air under ambient conditions. The diameter of the pendant droplets is about 360 ± 10 μm. The approach and retraction speed of the actuator is set to 11 mm/s, with a delay of less than 1 ms.

As solvent we used toluene (analytical grade, Sigma-Aldrich Chemical GmbH, Germany), which was deposited on 1.5 cm x 1.5 cm polystyrene (PS) substrates, cut from commercial 1.2 mm thick extruded PS plates (M_w = 284 kg·mol^{-1}, M_w/M_n = PDI (polydispersity index) = 2.6, GoodFellow GmbH, Bad Nauheim, Germany). First, the polymer substrates were cleaned with methanol (analytical grade, Sigma-Aldrich Chemical GmbH, Germany) in an ultra sonic bath for 15 min, after that rinsed several times with methanol and finally dried with filtered N_2 prior to use.

In order to ensure the best possible reproducibility of microstructuring, the initial volume of the pendant droplets was kept constant by automatically moving the piston inside the syringe with a speed of 10-100 μm/s to compensate for the solvent evaporation. Thereby, the droplet is visualized by a computer-controlled camera attached to a microscopic zoom objective. Per series, 20 identical toluene droplets were placed on a polystyrene substrate. After waiting for drop evaporation ($\sim$ 4s) and drying ($\sim$ 2h), the surface topology of the resulting microtopology in the polymer surface was imaged with a three-dimensional (3D) confocal white-light microscope of the disk-scanning type (μsurf$^{®}$, Nanofocus AG, Oberhausen, Germany). This equipment provides an excellent agreement with tactile systems but is less time-consuming.

3   Geometric Model

This section explains the mathematical model used for describing the raw data (*RD*). In a first approach the crater is assumed to be rotationally symmetric with respect to an axis going through the lowest point of the crater, the centroid. The parameters of the mathematical model describe the shape of the synthetic crater (*SC*) from which finally the global geometric parameters are derived. The data, originally provided in Cartesian coordinates (x, y, z), are transferred into a polar coordinate system with radius r and height h, where h is synonymous to z.

3.1   B-splines

On the condition of rotational symmetry, the profile of the crater is described by a B-spline [Prautzsch; Böhm and Paluszny (2001)] generating the shape. B-splines are curves that are governed by control points $\vec{D}_i = [r_i, h_i]$ being the parameters of our model. They can be easily calculated from piecewise polynomials (called base functions) using one path parameter τ (cf. 3.2). We used cubic B-splines consisting of cubic polynomials $N_i^{(3)}(\tau)$ (note that $^{(3)}$ is a superscript not an exponent):

$$\vec{D}(\tau) = \sum_i \vec{D}_i N_i^{(3)}(\tau) \tag{1}$$
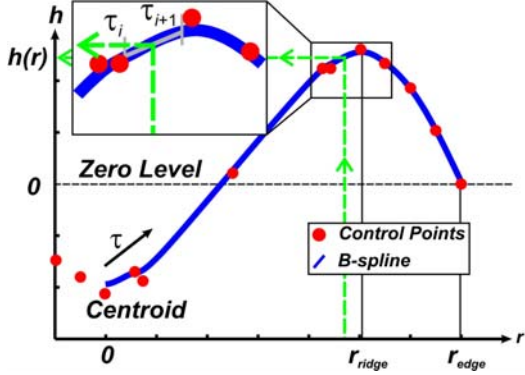
Figure 2: The height $h(r)$ to a given radius r is interpolated by a B-spline describing the profile from the centroid to the crater's edge along the path parameter τ. The spline is computed from piecewise polynomials in the intervals $[\tau_i,\ \tau_{i+1}]$ (inset). Note that the control points do not necessarily lie on the curve of the B-spline.

Here, $\vec{D}(\tau)$ defines the spline function, which maps the path parameter to the r and h coordinate of the spline. Note that the terminology of B-splines distinguishes between control points $\vec{D}_i$ (not necessarily lying on the curve) and interpolation points E_j lying on the curve (cf. 3.2 and Appendix I, Step 5). Given one set of points the other can be easily computed. However, Eq.(1) and the corresponding computational procedures become simplest if formulated with control points.

Cubic B-splines need a minimum of four control points $\vec{D}_i$. The more points are used, the more details of the shape can be resolved (cf. Appendix, step 5). A special feature of B-splines is the local influence of the control points on the spline: If one control point is moved, only a small section of the curve changes. This feature improves the convergence properties of the subsequently discussed parameter fitting algorithm.

3.2 Synthetic crater model

To describe the crater's profile by a form function we introduce a normalized radius

$$\bar{r} = r/r_{ridge} \text{ defined for } 0 \leq \bar{r} \leq r_{edge}/r_{ridge}. \quad (2)$$

Here r_{ridge} is the radius of the crater ridge and $r_{edge} > r_{ridge}$ is the radius where the outer crater wall passes over to the flat polymer substrate (Fig.2). Consequently, the highest point of the crater is always given by $\bar{r} = 1$. The two component functions of the B-spline $\vec{D}(\tau) = (D_{\bar{r}}(\tau), D_h(\tau))$ now implicitly define the wanted relation $h(\bar{r})$ between surface height h and normalized radius $\bar{r}$ (cf. Fig.2). By formally inverting the radius component function $D_{\bar{r}}(\tau)$, $h(\bar{r})$ is explicitly given by

$$\tau = D_{\bar{r}}^{-1}(\bar{r}) \Rightarrow h(\bar{r}) = D_h\left(D_{\bar{r}}^{-1}(\bar{r})\right) \quad (3)$$

Rotation of the profile $h(\bar{r})$ around the crater centroid then generates the rotational symmetric synthetic crater in the x-,y-,z-coordinate system. The height z of the synthetic crater is given by:

$$z = SC(x, y) = h(\bar{r}) = h\left(\sqrt{x^2+y^2}/r_{ridge}\right) \quad (4)$$

Here, the crater's centroid is assumed to be in the origin of the coordinate system ($[x_0, y_0] = [0, 0]$). Notice that the function SC is implicitly parameterized by the control points $\vec{D}_i$ which can be adaptively chosen later on for an optimal reproduction of the raw data (cf. Appendix, steps 6 and 7).

3.3 Elliptic craters

Measured craters frequently exhibit a slight ellipticity. To account for this feature the synthetic crater model is extended. The parameter ridge in Eq.(4) is replaced by two parameters r_{max} and r_{min} denoting the length of the principal axes (cf. Fig.3). Another new parameter is the rotation angle ϑ of the first axis w.r.t. the x-axis (Fig.3, left). Using these parameters ridge is redefined as a function of the angle $\varphi = \varphi(x, y)$:

$$r_{ridge} = \frac{r_{min}}{\sqrt{1 - \left(1 - (r_{min}/r_{max})^2\right)\cos^2(\varphi - \vartheta)}} \quad (5)$$

If $\varphi = \vartheta$ it follows that $\bar{r} = r/r_{ridge} = r/r_{max}$ as before (cf. Eq.(3)). If $\varphi = \vartheta + \pi/2$ it follows $\bar{r} = r/r_{ridge} = r/r_{min}$.

3.4 Fitting to the raw data

In order to fit the synthetic crater *SC* to the raw data *RD*, the discrepancy described by least squares is minimized w.r.t. the model parameters (cf. section *iteration step by re-adaptation of the B-spline parameters*):

$$\min\left(\sum_{i=1}^{n}|RD\,(x_i,y_i) - SC\,(x_i,y_i)|^2\right) \qquad (6)$$

Here, the complete measured data set $RD\,(x_i,y_i)$ is involved and the minimum is computed with respect to all parameters of the synthetic crater (i.e., (x_0,y_0), $\vec{D}_i$, r_{max}, r_{min}, ϑ).

Caused by the large number of experimental data compared to the relatively few parameters of the B-spline, the straight forward solution of the optimization problem described in Eq.(6) suffers from local optima, bad convergence and long computation times. For this reason a more sophisticated parameter fitting procedure has been implemented, which leads to a much faster and more reliable fitting. The technical details of this algorithm are described in Appendix I. Here, only the key ideas are given which are

1. to derive good starting values for the optimization problem given in (Eq.(6)) by a heuristic procedure based on the experimental data,

2. to choose the spline control points in an adaptive way by a different heuristics,

3. to use a robust optimization algorithm that avoids local optima in the neighborhood of the starting values.

3.5 Performance results

The run time of the applied optimizations is mainly determined by the time needed for one single evaluation of the optimization criterion in Eq.(6). It takes about 0.5 sec for the highly resolved data used in this investigation. Typically, an optimization algorithm with tight precision bounds will need about 500 runs for the optimization, resulting in several minutes of computation time needed for one crater. Three concrete algorithms have been compared:

1. A genetic algorithm (GA) [Chipperfield; Fleming; Pohlheim and Fonseca (1999)] proved to have outstanding ability to find good optima. GAs imitate the process of biological evolution: During each successive generation, the current individuals are used to breed a new generation by applying so called genetic operators. Subsequently, new individuals are selected through a fitness-based process. This procedure is repeated until a termination condition has been reached [Goldberg (1989)]. The drawback of this global search strategy is a very long computation time in the order of half an hour per crater. However, these results were taken as reference for faster algorithms.

2. The gradient-based *fmincon* optimization routine of MATLAB needs a large number of additional function evaluations to evaluate parameter sensitivities numerically. This results in rather long compute times with still lower accuracy than the GA results.

3. Finally, the simple gradient free Nelder-Mead simplex algorithm implemented in MATLAB's *fminsearch* routine provided a good trade off between precision and compute time. It takes about 3 minutes to find the optimum with only one digit of precision less than the GA.

If compute time becomes limiting, an adaptation of the presented tool for a many processor computing cluster is straight forward and has, in fact, already be used in this investigation.

The achievable precision of the tested optimization algorithms were checked by generating different synthetic surfaces with added noise. Even in the presence of rather unrealistic 5% noise levels the major parameters (centroid, axis length) could be reproduced with almost 3 digits of precision (best algorithm). Other parameters and the crater profiles were reproduced with two digits. However, in case of almost circular craters (i.e. $r_{min} \approx r_{max}$) the fitted rotation angle ϑ can be completely meaningless – as expected in this situation.

Finally, the influence on the initial parameter guesses on the final result has been tested. Since the GA is initialized by small random perturbations of the previously computed initial parameters it could be verified by repeated optimization runs that this algorithm always converged to the same result.

The resolution of the underlying scans is rather high. In fact, the algorithm will apply to much smaller craters. Clearly, the limit is reached when the pixel resolution is not more than about 10 times lower than the crater radius because in this case the crater profiles cannot be precisely resolved anymore. In this case an AFM might help which supplies even more data.

3.6 Determination of global geometric parameters

In the model fitting step a first data compression of the raw data is performed, because the whole crater can be described by a few parameters. Since these parameters, apart from the ellipse principal axes, are hard to interpret in practice, we condense the data even more by introducing some meaningful global geometric parameters (Fig.3, cf. Tab.1), which are also used for the statistical evaluation. Computational details can be found in Appendix III.

4 Serial Analysis

As a demonstration for the analysis of a large number of craters, Fig.4 and Table 2 show the results of a serial evaluation of two sets of experiments with 20 craters each, generated with an identical experimental setup (cf. chapter 2, section *experimental setup und evaluation*). Since highest priority has been given to the computation of globally optimal results the Genetic Algorithm has been chosen for the following investigation.

4.1 Global evaluation of two experimental series

A comparison of each synthetic crater with the associated original crater was done by means of the χ^2-test for non linear regression models with known measurement error variance [Seber and Wild (1989)]. For the calculation of the confidence interval for each data point an error of 5 percent of the maximum ridge height of all craters of each series is assumed. Taking a confidence of 90 percent, 10 percent of false negatives have to be expected for this test. As a result, for each experimental series at least 85 percent of the synthetic craters show χ^2-values within the required confidence interval. This confirms an excellent reproduction of all craters by the synthetic model.

Moreover, the χ^2-test was passed only if an elliptic cross-section for the synthetic craters was assumed, proving that the original experimental data represent elliptic craters.

4.2 Comparison of the two experimental series

As Fig.4 and Table 2 show, the craters of the second experiment are higher but have slightly smaller diameter than in the first experiment. Nevertheless, they agree well with the droplet width of $360\,\mu$m. The principal axes are about 14 μm smaller in experiment 2, but the ridge height (RH) and the crater depth (CD) are 1 μm and 0.7 μm larger in experiment 2, respectively. Thus, the edge of the crater appears to be shifted vertically with respect to the flat substrate surface outside the crater. This assumption is validated by the volume of the crater subsurface (V_{CS}), which in experiment 1 is nearly twice as large as in experiment 2. Interestingly, the volumes of the crater wall (V_{CW}) are approximately equal, whereas the volume of the interior (V_I) is about 13000 μm^3 bigger in experiment 2. However, this is in the order of the error of each single set of experiments.

The inclination at the crater edge (I_{CE}) and the inner inflection point (I_{IIP}) for the two sets of experiments are comparable, whereas the tangent in the outer inflection point (I_{OIP}) shows a steeper crater shoulder in experiment 2. This can also be seen in Fig.4. The aspect ratio (AR) of 0.012 and 0.015, respectively, are typical for the structuring of polymer substrates by the above described drop deposition technique (chapter 2; [Haschke; Graf; Bonaccurso; Li; Suttmeier and Wiechert (2006)]). The small differences in both generations show again that the craters are comparable, although they differ in height, depth and diameter.

Table 1: Global geometric parameters and their description (cf. Fig.3)

| Abbr.	Global geometric parameters	Description
	Crater dimensions	
r_{max} r_{min}	• Length of the principal axes	Major and minor principal axis
r_{ridge}	• Radius of the ridge	Radius at the crater's ridge (highest point)
r_{edge}	• Radius of the edge	Radius at the crater's transition to the unchanged substrate
Centroid	• Position of the minimum of the crater	Minimum and origin of the crater
RH	• Ridge height	Difference between the B-spline's maximum and the unchanged substrate (zero level)
CD	• Crater depth	Difference between the B-spline's maximum and its minimum (centroid)
AR	• Aspect ratio	Defined as quotient of the crater's depth and the mean length of the principal axes of the ellipse
	Volume of the	
V_I	• Interior	Realized as numerical integration of a rotational solid described by the B-spline
V_{CW}	• Crater wall	Volume above zero-level inside the crater's wall, realized by a numerical integration
V_{CS}	• Crater subsurface	Volume below zero-level (inside the crater), realized by a numerical integration
	Inclination	
I_{CE}	• Crater edge	Inclination of the tangent to the crater's outer shoulder at the transition to the unchanged substrate (given as angle to the horizontal)
I_{OIP}	• Outer inflection point	Inclination of the tangent in the inflection point of the outer crater shoulder (given as angle to the horizontal)
I_{IIP}	• Inner inflection point	Inclination of the tangent in the middle inflection point of the inner crater shoulder (given as angle to the horizontal)
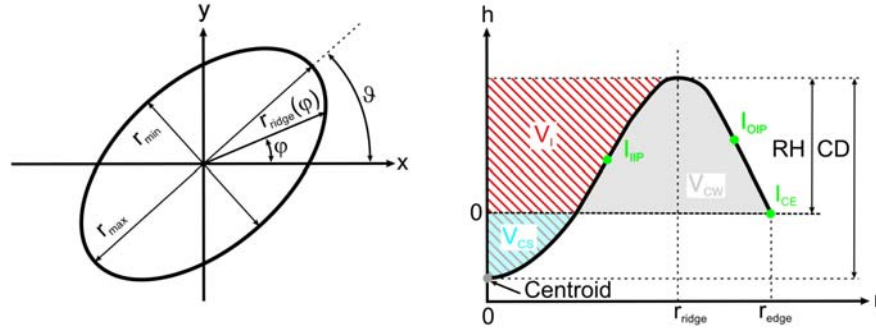
Figure 3: Global geometrical parameters for an elliptic crater shape (left) and for the resulting crater profile (right). For abbreviations, see table 1.

Table 2: Statistical evaluation of two sets of experiments with 20 craters each (derived from the synthetic craters in fig. 9). The deviations shown are the maximum relative deviations from the mean value of each experimental series.

	Experiment 1				Experiment 2			
	Mean		Deviation		Mean		Deviation	
• r_{max}	172.2	μm	±7	%	157.0	μm	±8	%
• r_{min}	166.9	μm	±5	%	152.5	μm	±7	%
• RH	3.2	μm	±6	%	4.2	μm	±9	%
• CD	4.1	μm	±6	%	4.8	μm	±9	%
• AR	0.012		±7	%	0.015		±9	%
• V_I	119591	μm^3	±14	%	132543	μm^3	±14	%
• V_{CW}	262922	μm^3	±19	%	268560	μm^3	±26	%
• V_{CS}	4893	μm^3	±24	%	2653	μm^3	±69	%
• I_{CE}	-8.3	°	±28	%	-8.3	°	±35	%
• I_{OIP}	-8.6	°	±11	%	-11.7	°	±12	%
• I_{IIP}	2.1	°	±8	%	2.6	°	±9	%

A hint for the origin of these differences might come from the slightly higher angles observed in experiment 2, especially the angle at the outer inflection point I_{OIP} of the craters. If we assume that this angle reflects the contact angle of the droplet at the end of the evaporation, a higher angle would lead to a higher vertical component of the stress from the surface tension acting on the soft, swollen polymer surface. This in turn leads to a higher pile-up at the ridge of the crater and thus could explain the observed difference between the two sets of experiments. The difference in the contact angles is reasonable, since the polymer substrate is a commercial product with a very broad distribution of the molar mass.

In both sets of experiments the volume of the crater wall is much higher than the volume of the subsurface. This means that polymer is not just moved from the centre to the edge, which would lead to a conservation of mass and volume, but must have permanently taken up solvent molecules. This was observed earlier [Li; Höhn and Graf (2006)].

The deviations in Table 2 are calculated by averaging over the 20 synthetic craters within each set. It is obvious that the deviations of all global geometrical parameters dealing with the crater dimensions are equal or below 10 percent, which is
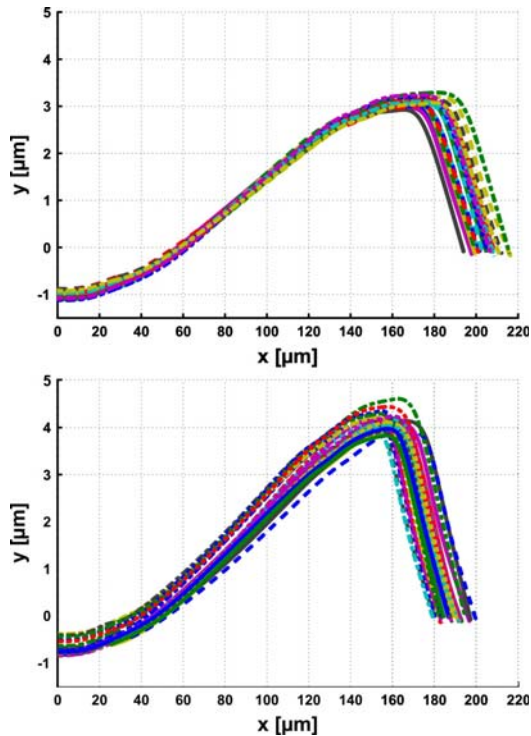
Figure 4: Synthetic crater profiles of two experimental series with 20 craters each: experiment 1 (top) and experiment 2 (bottom).

in the range of the experimental errors, i.e. the initial droplet volume and the contact area between droplet and polymer surface. The same applies for the deviation of I_{OIP} and I_{IIP}.

The greater deviation for the interior and the crater edge volume of about 15% is reasonable, since errors in length should lead to a threefold error in volume, according to error propagation.

The big deviations of the crater's subsurface volumes V_{CS} with up to 70 percent are related to outliers for one crater in each generation. Interestingly, the other global geometrical parameters of these two craters are within the common deviations so that here no explanation for the outliers can be given.

The deviation of the inclination at the crater's edge of about ± 30% is due to the fact that one cannot precisely determine the transition from the crater's outer shoulder to the unchanged substrate (cf. Fig.9). Thus, the tangent is not calculated under the same restrictions for all craters.

The comparison between the two sets shows that the deviation between nearly all parameters is bigger than the deviation within one set. This reflects the fact that a polymer substrate from a different batch was used for the second experiment and parts of the droplet dispenser, as e.g. the syringe, were rearranged in between. Therefore, the statistical analysis of different sets of experiments reveals how well the experimental parameters can be controlled. In turn, it shows how sensitive the physical processes determining the final surface structure are influenced by the experimental boundary conditions.

5   Conclusion and Outlook

We presented a profile analysis tool for regularly microstructured surfaces, which occur, for example, after the evaporation of toluene droplets on a polystyrene substrate. The resulting microcraters are characterized by a B-spline describing the craters profile under the assumption of a slight ellipticity. The achieved synthetic craters are adjusted to the original craters by means of a full least squares fitting. Subsequently to the fitting procedure a statistical analysis is performed with the help of global geometrical parameters characterizing the shape of the craters.

The results show that the presented tool is suitable for an efficient, highly automized analysis of microstructured surfaces. The demands on the tool regarding comparability of original and synthetic craters and, above all, the data reduction are met. The deviation of synthetic and original crater profiles w.r.t. the crater dimensions is in the range of the experimental errors, so that a sufficient comparability is achieved. For the description of a crater profile with a B-spline a total of 35 parameters are necessary, accumulating to only ~ 240 Bytes per dataset. This is equivalent to a data compression rate of approximately 67,000 : 1. The analysis of two sets of microstructures with 20 datasets each, proofs it usage for high throughput serial analysis.

Coming along with the analysis of a series of experimental data the included statistical analysis is furthermore able to estimate the process accuracy and the process assurance of the experimen-

tal setup. The small deviation of the synthetic craters compared to that with the original craters and, above all, of the synthetic craters compared to each other demonstrates the high process accuracy in the example.

Therewith, the profile analysis tool can also be used for studying the stochastic influences of process parameters on experiments on the microscale and to analyse the influence of experimental parameters on the crater profile empirically. This is not only interesting for basic research to understand the structure formation in polymer surfaces, but also for industrial applications, especially with focus on Lab-on-Chip applications. There the shape of microvessels and -lenses have to be controlled on a micrometer scale.

In conclusion, we developed an analysis tool not only for experimenters but also for industry because one can quickly and easily gain control over the fabrication of microstructured surfaces by determine geometrical parameters to the point of judging the process accuracy.

However, it should be mentioned that the profile analysis tool at its current state is not operating completely automatic as it would be required for quality control in an industrial production process. It still needs a brief manual inspection of the results (e.g. by using a graphical display as in Fig.1, bottom). Essentially, two features are missing:

1. If the microstructures may not be arranged on a regular grid (as in Fig.5) an overlap of structures possibly has to be taken into account. This can easily be tested by checking the niveau lines in Fig.5 (bottom) for intersections.

2. If there is a gross deviation of a microstructure from the regular shape this can be directly seen from a large χ^2 value (cf. section 4.1).

Clearly, the general approach of the presented method is not restricted to craters or rotationally symmetric structures and thus can be modified for other types of symmetric profiles, such as arrays of rectangular vessels [Bonaccurso; Butt and Graf

(2004)], where the geometry shows other symmetries. In this case a different synthetic surface model has to be chosen. Moreover, the developed tool might also be applied to macroscopic structures. However, in this case the aims are usually quite different (see introduction).

References

Alberdi, A.; Merino, S.; Barragia, J.; Aranzabe, A. (2004): Microstructured Surfaces for Tribological Applications, In: Proceedings of *Tribology and Lubrication Engineering*, T. A. Esslingen (Eds.), Eibar, Spain, 13.-15.01.2004.

Benitez, P.; Minano, J.C.; Hernandez, M. (2004): On the Analysis of Microstructured Surfaces, In: Proceedings of "*Nonimaging Optics and Efficient Illumination Systems*", R. Winston and R. J. Koshel (Eds.), Denver, Colorado, USA, 02.-04.08.2004, publ. by Proceedings of the SPIE Vol. 5529, Bellingham, Washington, USA.

Benitez, P.; Minano, J.C.; Santamaria, A. (2006): Analysis of Microstructured Surfaces in Two Dimensions, In: *Optical Science of America*, Vol. 14, Iss. 19, pp. 8561-8567.

Bonaccurso, E.; Butt, H.-J.; Graf, K. (2004): Microarrays by Structured Substrate Swelling, In: *European Polymer Journal*, Vol. 40, Iss. 5, pp. 975-980.

Bonaccurso, E.; Butt, H.-J.; Hankeln, B.; Niesenhaus, B.; Graf, K. (2005): Fabrication of Microvessels and Microlenses from Polymers by Solvent Droplets, In: *Applied Physics Letters*, Vol. 86, Iss. 12, pp. 124101.1-124101.3.

Bonaccurso, E.; Graf, K. (2004): Nanostructuring Effect of Plasma and Solvent Treatment on Polystyrene, In: *Langmuir*, Vol. 20, Iss. 25, pp. 11183-11190.

Genetic Algorithm TOOLBOX For Use with MATLAB - Version 1.2 (1999): by Chipperfield, A.; Fleming, P.; Pohlheim, H.; Fonseca, C., De-

partment of Automatic Control and System Engineering, University of Sheffield, UK.

Deegan, R.D.; Bakajin, O.; Dupont, T.F.; Huber, G.; Nagel, S.R.; Witten, T.A. (1997): Capillary Flow as the Cause of Ring Stains from Dried Liquid Drops, In: *Nature*, Vol. 389, pp. 827-829.

Goldberg, D. E. (1989): Genetic Algorithms in Search, Optimization and Machine Learning, 1. edition, 432 pages, Addison-Wesley Longman, Bonn.

Haschke, T.; Graf, K.; Bonaccurso, E.; Li, G.; Suttmeier, F.-T.; Wiechert, W. (2006): Evaporation of Solvent Microdrops on Polymer Substrates: Crater Geometries and Parameter Sensitivity Analysis, In: Proceedings of *Second International Conference on Transport Phenomena in Micro and Nanodevices*, M. Gad-el-Hak (Eds.), Barga, Italy, publ. by CD Publication, Engineering Conference International, Brooklyn, New York.

Haschke, T.; Wiechert, W.; Graf, K.; Bonaccurso, E.; Li, G.; Suttmeier, F.-T. (2007): Evaporation of Solvent Microdrops on Polymer Substrates: From Well Controlled Experiments to Mathematical Models and Back, In: *Nanoscale and Microscale Thermophysical Engineering*, Vol. 11, Iss. 1, pp. 31-41.

Hoßfeld, W.; Wittwer, V.; Nitz, P.; Gombert, A.; Bläsi, B.; Bühler, C.; Walze, G.; Georg, A. (2003): Application of Microstructured Surfaces in Architectural Glazings, In: Proceedings of *Glass Processing Days, 8th International Conference on Architectural and Automotive Glas 2003*, J. Vitkala (Eds.), Tampere, Finland, June 15 - 18, 2003.

Ichikawa, Y.; Toriwaki, J.-I. (1996): Confocal Microscope 3D Visualizing Method for Fine Surface Characterization of Microstructures, In: Proceedings of *Flatness, Roughness, and Discrete Defect Characterization for Computer Disks, Wafers, and Flat Panel Displays II*, J. C. Stover (Eds.), Denver, Colorado, USA, publ. by Proceeding of SPIE Vol. 2862, Bellingham, Washington, USA.

Kagerer, B.; Brodmann, R.; Valentin, J.; Filzek, J.; Popp, U. (2002): 3D-Confocal Mi-

croscopy for Surface Analysis of Microstructured Materials, In: Proceedings of *Optical Scanning 2002*, S. F. Sagan; G. F. Marshall and L. Beiser (Eds.), Seattle, Washington, USA, publ. by Proceedings of SPIE Vol. 4773, Bellingham, Washington, USA.

Krol, S.; Nolte, M.; Diaspro, A.; Mazza, D.; Magrassi, R.; Gliozzi, A.; Fery, A. (2005): Encapsulated Living Cells on Microstructured Surfaces, In: *Langmuir*, Vol. 21, Iss. 2, pp. 705-709.

Li, G.; Butt, H.-J.; Graf, K. (2006): Microstructures by Solvent Drop Evaporation on Polymer Surfaces: Dependence on Molar Mass, In: *Langmuir*, Vol. 22, Iss. 26, pp. 11395-11399.

Li, G.; Höhn, N.; Graf, K. (2006): Microtopologies in Polymer Surfaces by Solvent Drops in Contact and Noncontact Mode, In: *Applied Physics Letters*, Vol. 89, Iss. 24, pp. 241920.1 - 241920.3.

Lipowsky, R. (2004): Wetting Morphologies at Structured Surfaces, In: *Jahresbericht 2003 / 2004*, Max-Planck-Institut für Kolloid- und Grenzflächenforschung, Potsdam.

Magnani, A.; Priamo, A.; Pasqui, D.; Barbucci, R. (2003): Cell Behaviour of Chemically Microstructured Surfaces, In: *Material Science and Engineering: C*, Vol. 23, Iss. 3, pp. 315-328.

MatLab R2006a (2007): by The Mathworks Inc., Natick, Massachusetts, USA.

Osfouri, S.; Stano, P.; Luisi, P.L. (2005): Condensed DNA in Lipid Microcompartments, In: *Journal of Physical Chemistry B*, Vol. 109, Iss. 42, pp. 19929-19935.

Prautzsch, H.; Böhm, W.; Paluszny, M. (2001): Bezier and B-Spline Techniques, 1. edition, 304 pages, Springer Verlag, Berlin.

Seber, G. A. J.; Wild, C. J. (1989): Nonlinear Regression, 1. edition, 800 pages, John Wiley & Sons Inc., New York, USA.

Seemann, R.; Brinkmann, M.; Kramer, E.J.; Lange, F.F.; Lipowsky, R. (2004): Wetting Morphologies at Microstructured Surfaces, In: *Proceedings of the National Academy of Science*, Vol. 102, Iss. 6, pp. 1848-1852.

Shastry, A.; Case, M.J.; Böhringer, K.F.

(2006): Directing Droplets Using Microstructured Surfaces, In: *Langmuir*, Vol. 22, Iss. 14, pp. 6161.1-6161.7.

Sirringhaus, H.; Kawase, T.; Friend, R. H.; Shimoda, T.; Inbasekaran, M.; Wu, W.; Woo, E. P. (2000): High-Resolution Inkjet Printing of All-Polymer Transistor Circuits, In: *Science*, Vol. 290, Iss. 5000, pp. 2123-2126.

Stupperich-Sequeira, C.; Graf, K.; Wiechert, W. (2003): Modeling of the Production of Microwells, In: Proceedings of *4th Mathmod*, I. Troch and F. Breitenecker (Eds.), Vienna, Austria, 05.-07.02. 2003, publ. by Conference Proceedings "4th Mathmod" in: ARGESIM-Reports, Vienna, Austria.

Stupperich-Sequeira, C.; Graf, K.; Wiechert, W. (2006): Modeling and Simulation of Microwell Formation, In: *Mathematical and Computer Modelling of Dynamical Systems*, Vol. 12, Iss. 4, pp. 263-276.

Valentin, J. (2006): Mikrooptiken optisch vermessen, In: *Sonderdruck aus der Fachzeitschrift "Mikroproduktion"* (Vol. 2/2006), pp. 1-4.

Appendix Profile Analysis Procedure

Part I:

Pre-processing and determination of parameter starting values

Step 1 Identifying the craters within the raw data matrix

A set of raw data typically consists of 20-30 different microcraters received on one polymer surface (Fig.5, top). They are arranged in a matrix (crater matrix) for reasons of a practicable experimental procedure and analysis.

The surface is represented by a table containing three columns for *x*-, *y*-, and *z*-coordinates (height information). Since for calculations only one crater at a time is needed, the first step is to identify each of the craters within the crater matrix and extract them into single files. As a result a given crater matrix consisting of *n* craters is cut into *n* single parts (Fig.5, bottom). For reasons of simplicity, the algorithm used for the identifica-

tion of the craters converts the crater matrix into a pixel matrix. A re-transformation for an arbitrary data point to the origin metric coordinates is easily manageable by knowing the scanning solution.

Identifying the parts of the crater matrix belonging to one single crater, the raw data of each crater are stored separately, containing the *x*- and *y*-coordinates of the sample and the corresponding *z*-values, arranged in a matrix. These pixel matrices are used for calculations and shown in the following figures.
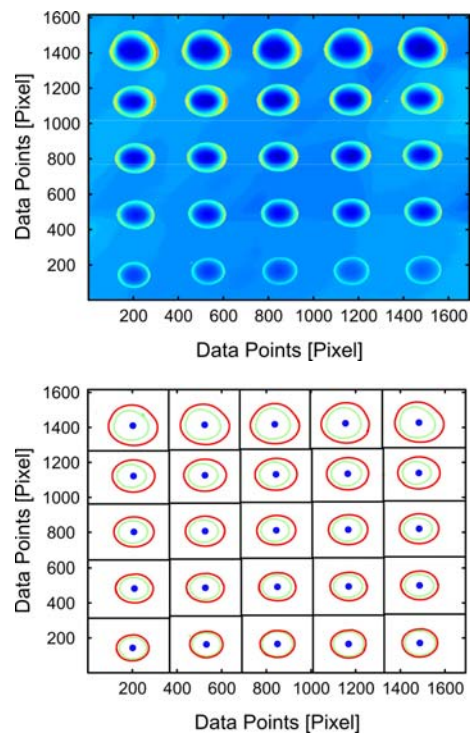

Figure 5: Principle of identification of single microcraters within an arbitrarily set of 25 craters in a matrix. Top: Top view of the crater matrix. The z-values are represented by different colours (blue ≡ low, red ≡ high). Thus, the craters can be well distinguished from the unmodified substrate surface (lighter blue). Bottom: Identified craters (green) with convex hull (red) and centroid (blue). The black lines mark the area belonging to each crater. Note that on the *x*- and *y*-axis pixel and not Cartesian coordinates are shown.

Step 2 Smoothing of experimental noise

Usually, experimental data (*RD*) contain noise such as spikes (Fig.6, top), which can have different origin like impurities on the substrate or artefacts from the experimental technique. Owing to the assumption of a symmetric crater described by a smoothed B-spline, these effects are treated as outliers and thus are discarded.
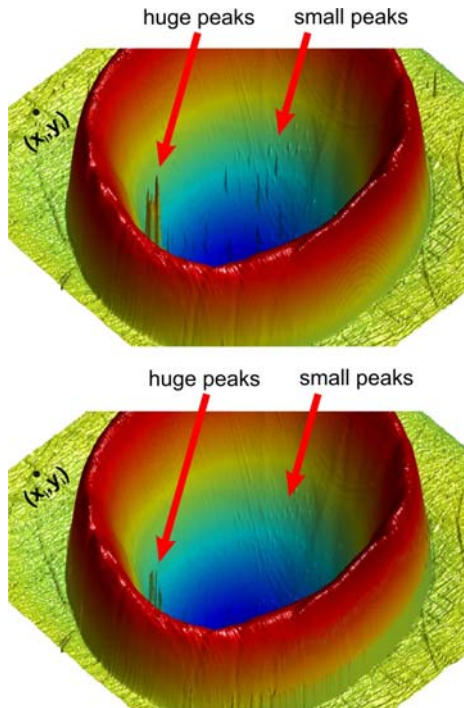

Figure 6: Crater with optical artefacts (top) and after smoothing with the median filter (bottom). Note that smaller peaks are completely removed, whereas huge peaks persist with a decreased height.

For this reason, these peaks are smoothed by a median filter: A local data window with a radius of 4 pixels scans the data matrix considering only those pixels lying completely inside the circle (dark green pixels in Fig.7) and the result is written into a new matrix. In the next step, the original data are compared with this smoothed matrix and data points, which differ more than five percent from the crater's height at r_{ridge}, are discarded in the original matrix. The missing height data are calculated by linear regression. In this manner, smaller peaks are completely smoothed (cf.

upper right part of the craters in Fig.6), whereas huge peaks will persist with a decreased height (cf. lower left part of the craters in Fig.6). The resulting crater is shown in Fig.6 (bottom).
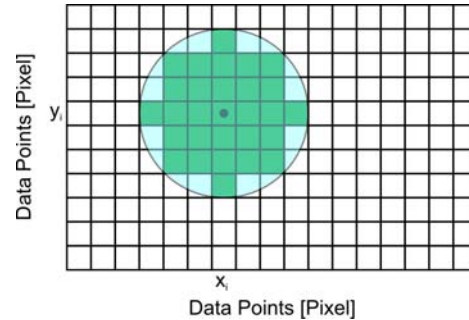

Figure 7: Scanning the data matrix with a circular window (the window is the total area of the dark green pixel). The matrix represents the x_i-values (columns) and the y_i-values (rows) in unit pixel. Within each square a z-value is given (not shown), which represents the height from Fig.6.

Step 3 Identifying the crater's centroid

As the crater can be considered as nearly rotationally symmetric, the crater's centre (centroid; cf. Fig.3) has to be found. To this end, the minimum of the whole z-value matrix is determined. However, this estimate is highly sensitive to noise. Thus, the position is adjusted by determining its distance to the ridge in *x*- and *y*-direction and moving the centroid along both axes, so that it is centred in relation to the ridge. The determined position of the crater is the starting value for the later optimization process (cf. *Part II*).

Step 4 Cutting of defined profiles

In the next step the B-spline describing the synthetic crater must be determined. For this several height profiles are extracted along rays starting from the previously found centroid and ending at the edge of the pixel matrix (cf. Fig.8). The edge is the transition from the crater's outer shoulder to the unmodified substrate. The number of rays can be variable; here eight rays with an incremental angle of 45 degrees were used. The height values of the pixels along the ray (dark blue pixels in

Fig.8) are collected into a data vector, describing the craters profile along this rotation angle.
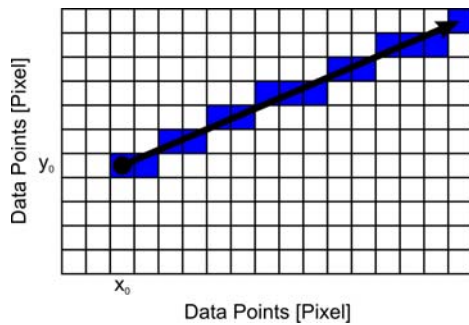

Figure 8: Cutting of height profiles within the pixel matrix along a ray outgoing from the centroid (x_0, y_0).

Every profile is now analyzed to find the crater's maximum and edge. The maximum along each profile can be found easily, whereas determining the edge needs a little more effort.

Here, we use a sliding regression predictor: Starting from the end of the above collected data vector, a fixed number of adjoined data points is used to calculate a straight line by linear regression. As long as the next data point outside this data-point-window differs less than 2 percent of the crater's depth from this line, the window is moved by one data point and the calculation starts again. If the data point differs more than 2 percent of the crater's depth from the line, the crater's edge is found (Fig.9, top).

Knowing the maximum height at r_{ridge} and the heights at r_{edge}, the crater's total height (as maximum of all z-values) and the craters diameter can be calculated for each profile, because the origin of the coordinate system was set to the centroid (cf. Fig.3).

The individual diameters of each of the eight profiles are used to roughly determine the principal axes r_{max}, r_{min} and the rotation angle ϑ of the elliptic crater according to Eq.(5). After that the elliptic shape is converted into a circular one by scaling all profiles along the abscissa such that each maximum has a distance of 1 from the origin (Fig.9, bottom; cf. section *geometrical model*). Now, these eight profiles are used for the pre-
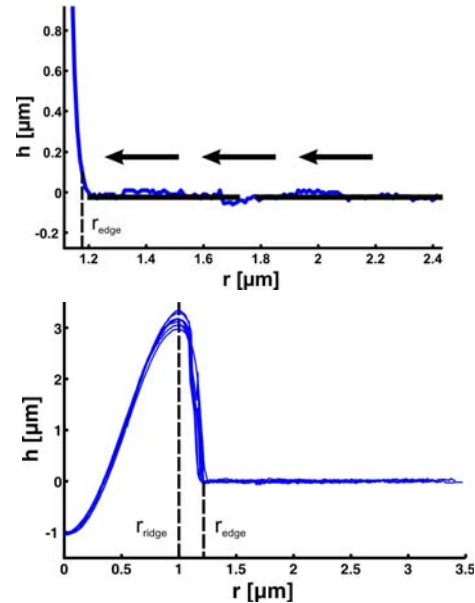
fitting of the raw data.

Figure 9: Top: identifying the crater's edge with the sliding regression predictor (evaluation starts at the right). Bottom: example of cut height profiles with maximum ridge height scaled to distance 1 from the origin.

Step 5 Pre-fitting of the raw data with a B-spline

The shape of each of the eight profiles is now approximated by a cubic B-spline (cf. chapter 3, section *geometrical model*). Therefore, we distribute so called interpolation points from which the control points are computed by means of a linear system of equations. Here, 12 interpolation points are specified in the following way: three points are uniformly distributed on the outer shoulder of the crater, i.e. the part from the maximum height of each profile to the edge of the considered profile. One interpolation point is set to the centroid, the maximum z-value and the middle between both, respectively. The remaining points are distributed near the crater's centroid and around the ridge since there are more changes of the B-spline to describe than in the rest of the crater.

After solving the linear system of equations there is a set of control points for each profile. As the

crater shall be described by only a single B-spline, the average over the eight profiles is calculated for each control point. This averaged B-spline describes the crater's shape along the eight profiles in good accordance to the experimental data. Thus, these values are used as starting point for the subsequent following fine-fitting within the optimization routine.

Part II:

Parameter fitting procedure (Optimization)

Step 6 Comparison of raw data (RD) and synthetic crater (SC) (full least squares fitting)

Up to now a sequence of heuristically rules were applied that allow guessing a good starting profile for the subsequent least squares fitting with the full data set. Equation (6) can now be solved with a relatively low computational effort because only the fine tuning of the parameters has to be done. In total, the fitting problem has 35 parameters (control points, crater centroid, principal axes of the ellipse, ellipsoid angle), which depend on each other. Using the initially determined parameter values (Part I, steps 2–5) the full synthetic crater is now generated by Eq.(4) and (5), respectively. These synthetic data are now compared with the raw data by means of full least squares fitting (cf. Eq.(6)).

Step 7 Iteration step by re-adaptation of the B-spline parameters

The sum of least squares, representing the difference between the synthetic crater and the original crater, is now minimized my means of a Genetic Algorithm [Chipperfield; Fleming; Pohlheim and Fonseca (1999)] available for Matlab. The Genetic Algorithm (GA) was chosen because of its ability of handling a large number of possible parameter configurations. Therefore, the GA re-adapts the 35 parameters of the B-spline in order to minimize the discrepancy between *SC* and RC data.

A further reason for choosing the Genetic Algorithm is that it is much more robust than gradient based optimization algorithms. Particularly, lots of local optima lie close to the true optimum

of the least squares problem. By using the GA a good reproducibility of the automatically computed results was obtained. The parameter fitting procedure is stopped after convergence of the sum of least squares, which is the case after 100 cycles in all cases. The found synthetic crater describes the original crater (*RD*) in best accordance and is used for the statistical analysis.

Part III:

Statistical Evaluation

Step 8 Determination of global geometric parameters

Most of the parameters defined in chapter 3.6 can be computed in a straight forward manner from the fitted model. Maxima, minima and inclinations are determined analytically by deriving the spline functions (i.e. third order polynomials). The volumes are computed from the well known formula for curves rotated around the y-axis:

$$V = \pi \cdot \int_a^b x^2 \cdot f'(x)\,dx \tag{7}$$

This integral can also be computed analytically by integration over each interval $[\tau_i, \tau_{i+1}]$ of the B-spline (cf. Fig.2). The rather technical details are left out for brevity.

Step 9 Statistical analysis of synthetic craters

For each single crater the goodness of fit is tested by applying the standard χ^2-test for nonlinear regression models [Seber and Wild (1989)]. The test checks whether the computed sum-of-squares is tolerable.

The extracted geometrical information of each crater is subsequently used for the statistical evaluation of the whole series of craters. To this end standard descriptive statistics is performed to compute mean values and standard deviations of the crater population.